Chemical Science

Accepted Manuscript

This article can be cited before page numbers have been issued, to do this please use: L. Seikh, C. Das, A. Saini, G. Sabharwal, S. Guria, P. Majumder, M. S. Balakrishna, G. K. Lahiri and A. Dutta, *Chem. Sci.*, 2026, DOI: 10.1039/D6SC02569B.

ROYAL SOCIETY OF CHEMISTRY

rsc.li/chemical-science

DOI: 10.1039/D6SC02569B

Pendant Amine-Promoted Complete Eight-Electron Photoreduction of CO_2 to Methane by a Molecular Nickel Catalyst

Chandan Das[a], Liton Seikh[a], Abhishek Saini[a], Gazal Sabharwal[a], Somnath Guria, Piyali Majumder[a], Maravanji S. Balakrishna[a], Goutam K Lahiri[a], and Arnab Dutta*[a,b,c]

[a]Department of Chemistry, Indian Institute of Technology Bombay, Powai, Mumbai 400076, India

[b]Centre for Climate Studies, Indian Institute of Technology Bombay, Powai, Mumbai 400076, India

[c]National Centre of Excellence CCUS, Indian Institute of Technology Bombay, Powai, Mumbai 400076, India

* Email: arnab.dutta@iitb.ac.in

Abstract

Solar-driven CO_2 reduction offers a sustainable route to carbon neutrality by converting greenhouse gases into value-added fuels. Here, we report a secondary coordination sphere design strategy that directs CO_2 photoreduction selectivity toward methane (CH_4). A redox-active Ni complex (**C1**), incorporating two (6-amino-2-(phenylazo)pyridine) ligand with a pendant amine, exhibits markedly enhanced CH_4 selectivity compared to control complexes lacking the pendant $–NH_2$ group. Systematic evaluation of sacrificial donors, proton sources, and photosensitizers identified a dimeric Cu(I)-based photosensitizer (Cu-PS-1) as a cost-effective alternative to Ir-systems, achieving $TON_{CO2→CO}$ = 4789, $TON_{CO2→CH4}$ = 1130, and $TON_{CO→CH4}$ = 3102, rivalling Ir-PS-1. Operando UV-vis, FTIR, and EPR spectroscopy, together with DFT calculations, revealed a stepwise $8e^-/8H^+$ reduction pathway in which the pendant $–NH_2$ group stabilizes key COOH and CH_x intermediates through hydrogen bonding, lowering activation barriers and steering selectivity toward CH_4. These results establish OCS engineering as a powerful design principle for earth-abundant molecular catalysts and highlight new opportunities for selective CO_2-to-CH_4 conversion in artificial photosynthesis and carbon valorization.

Keywords: Solar-driven CO_2 reduction; Secondary coordination sphere; Nickel molecular complexes; Methane selectivity; Photocatalysis

Introduction

The growing demand for circularity and sustainable resources has highlighted the possibility of using carbon dioxide (CO_2) as a feedstock to produce fuels and fine chemicals. Given these developments, solar-driven CO_2 reduction offers a sustainable way to convert solar energy while simultaneously addressing global warming concerns.[1–5] Converting solar energy into

View Article Online
DOI: 10.1039/D5SC02569B

chemical energy is particularly appealing, as it enables long-term and reliable energy storage compatible with existing infrastructure. However, the CO_2 reduction step remains inherently slow due to the high thermodynamic stability of the molecule. Furthermore, achieving selectivity in the CO_2 reduction process is challenging due to the possibility of generating numerous carbonaceous products at variable oxidation states,[4] compounded by the rapid kinetics of the competing hydrogen evolution reaction (HER) under reductive conditions. To overcome these challenges, there is a growing need for efficient and selective catalysts that are both rationally designed and economically viable. Recent years have witnessed a growing interest in molecular catalysts that employ cost-effective first-row transition metals.[6–8] Among them, earth-abundant nickel has emerged as an attractive alternative to leading *4d* and *5d*-metal (such as palladium and platinum)-based catalysts.[9,10] Nickel can readily access multiple oxidation states, a property that underpins its catalytic versatility. Its central role in [NiFe] CO-dehydrogenases (CODHs), which facilitate the reversible conversion of CO_2 to CO, makes it a highly attractive candidate for photocatalytic CO_2 reduction.[11,12] Consequently, nickel complexes have been extensively explored as molecular catalysts for CO_2 reduction. A series of mononuclear Ni-based catalysts, including Ni-N_2S_2 complexes,[13,14] N-heterocyclic carbene (NHC) complexes,[15,16] Ni-macrocyclic[17–21], nickel polypyridine[22,23] and other Ni-based[24–26] complexes, have demonstrated the capability to convert CO_2 to CO via a $2e^-/2H^+$ pathway. These studies highlight how both photochemical and electrochemical approaches can be employed to achieve efficient CO_2 conversion using earth-abundant metal catalysts, sometimes even in the absence of metal-based photosensitizers. Despite these improvements, the production of fully reduced C1 species CH_4 from CO_2 and CO through the $8e^-/8H^+$ or $6e^-/6H^+$ pathways, respectively, remains a significant challenge. To date, only a limited number of studies have reported the production of CH_4 from CO_2 and CO using 3*d* metal-based catalysts via photochemical pathways. Robert and co-workers[27] pioneered this field by employing an Fe-based molecular catalyst for the photocatalytic production of CH_4 from CO_2 and CO in the presence of triethanolamine (TEOA) as an electron donor under 420 nm light irradiation, achieving turnover numbers (TON) of 367 for CO and 159 for CH_4, respectively (**Figure 1**). Later, the same group[28] extended this work with the modification of the photocatalytic conditions, using 5,10-di(2-naphthyl)-5,10-dihydrophenazine and 3,7-di(4-biphenyl)-1-naphthalene 10-phenoxazine as organic photosensitizers and TEOA as an electron donor with irradiation of 435 nm light (**Figure 1**). Recently, Delcamp and co-workers[16] have strategically designed a novel series of Ni-based catalysts featuring redox-active macrocyclic ligand bearing bipyridyl N-heterocyclic carbene. These catalysts achieved the conversion of CO_2 to CH_4 with

View Article Online
DOI: 10.1039/D5SC02569B

a TON of up to 19,000 in the presence of $Ir(ppy)_3$ as a photosensitizer (PS) and BIH as an electron donor under a solar-simulated light (**Figure 1**). Ir-based photosensitizers (Ir-PS) are widely utilized due to their high photo-stability, strong visible-light absorption, extended excited-state lifetime, and strong reducing strength of the excited state.[29,30] Yet, the prohibitive cost and synthetic complexity of Ir-based photosensitizers remain major barriers to their practical use in CO_2-to-CH_4 conversion. Hence, there is a growing demand for cost-effective and sustainable alternatives. Researchers are actively exploring replacements such as organic (π-conjugated chromophores),[31–34] Al-based,[35] and 3*d* metal-based photosensitizers.[36–39] Among these, organic photosensitizers have gained significant attention due to their strong light absorption, high fluorescence quantum yields, and extended excited-state lifetimes, making them promising substitutes for noble-metal-based PS.

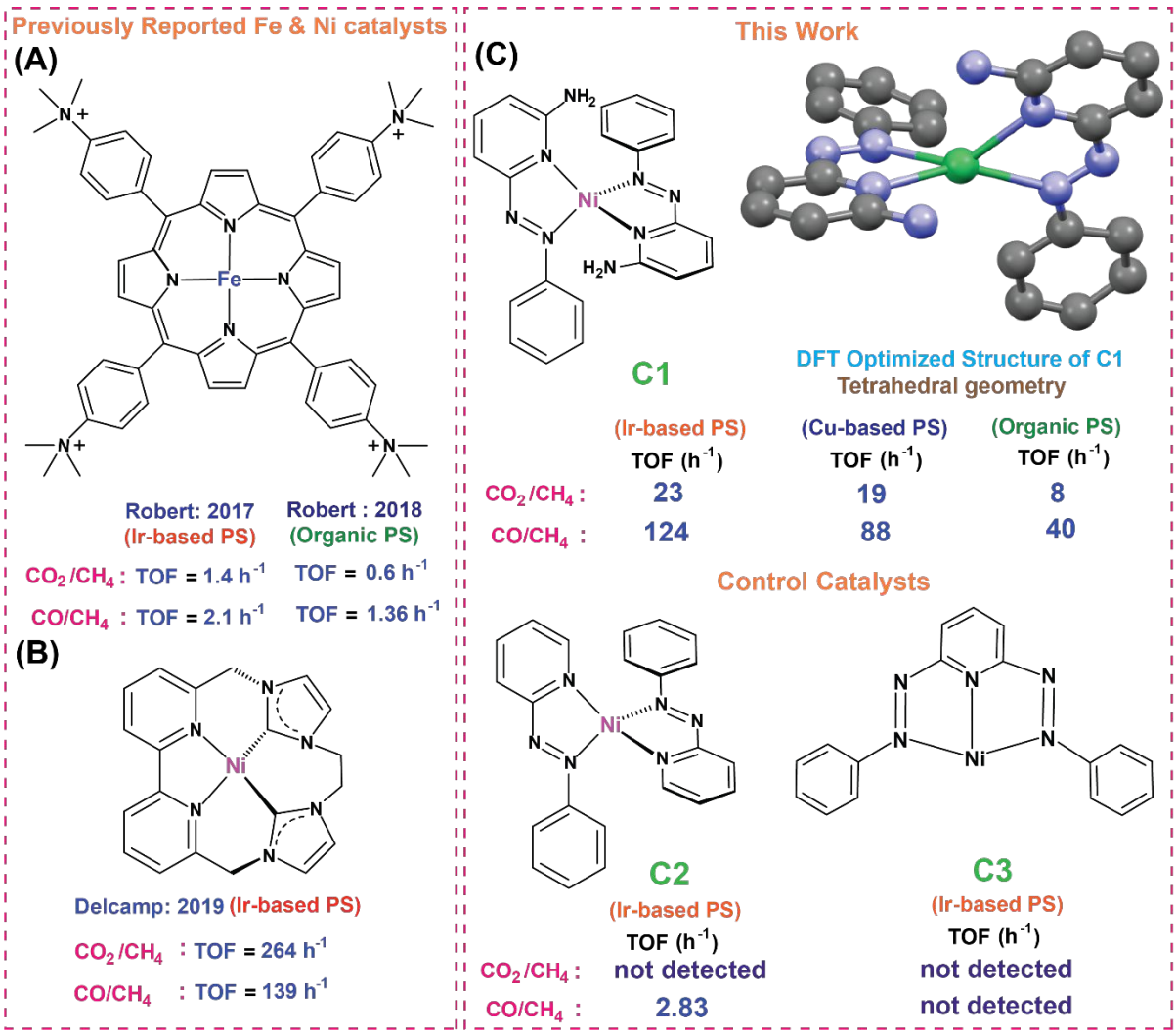

Figure 1. (A) Reported mononuclear Fe catalysts for photochemical CO_2/CO reduction reaction to CH_4. **(B)** Reported mononuclear Ni-based catalyst for photochemical CO_2/CO reduction reaction to CH_4. **(C) Present work**: Redox-active ligand-based Ni-catalysts **C1**: Ni-$(apap)_2$, **C2**: Ni-$(pap)_2$, and **C3**: Ni-$(dipap)_2$.

View Article Online
DOI: 10.1039/D6SC02569B

Copper(I)-based photosensitizers (Cu-PS) have gained prominence owing to their excellent photophysical properties and high earth abundance. The d^{10} configuration of Cu(I) prevents metal-centred excited states, resulting in strong luminescence and long-lived excited states.[40] Ishitani and co-workers demonstrated that binuclear heteroleptic Cu(I) photosensitizers exhibit significantly extended excited-state lifetimes (>10 μs) and greater oxidative power than their mononuclear homoleptic analogues.[41] In parallel, Dey and co-workers reported that a secondary coordination sphere interactions in an Fe-based molecular catalyst enabled selective electrochemical conversion of CO to CH_4.[42] These studies emphasize the critical role of ligand design and secondary coordination effects in modulating catalytic activity and selectivity of CO_2 and CO reduction.

This study explores a Ni-based molecular catalyst strategically designed to assess the influence of a pendant second-sphere amine group on the electrochemical and photochemical reduction of both CO_2 and CO to CH_4. A Ni-based complex (**C1**) was synthesized using two equivalents of the redox-active ligand 6-amino-2(phenylazo)pyridine) [**apap**], incorporating amine functionalities in the secondary coordination sphere. To systematically investigate its role, two additional Ni-based catalysts, **C2** and **C3**, were synthesized, lacking the a pendant second-sphere amine group but retaining similar primary coordination geometry. Photocatalytic CO_2 reduction reactions were conducted in CO_2-saturated organic solvents under visible light irradiation (440 nm), while probing a range of combinations of sacrificial electron donors, proton sources, and photosensitizers (PS). The study evaluated a diverse range of photosensitizers, including Ir-based (**Ir-PS-1**, **Ir-PS-2**), organic (**Cz-IPN**), and newly developed **PN(H)N** ligand-containing binuclear Cu(I) PS with varying halogen bridges (Cl: **Cu-PS-1**, Br: **Cu-PS-2**, I: **Cu-PS-3**). Notably, **Cu-PS-1** emerged as a highly stable and efficient photosensitizer, demonstrating superior TON compared to organic PS and serving as a promising cost-effective alternative to Ir-based PS. It achieved the apex in the optimized conditions with $TON_{CO_2 \rightarrow CO}$ (4789), $TON_{CO_2 \rightarrow CH_4}$ (1130) and $TON_{CO \rightarrow CH_4}$ (3102), closely following the performance of **Ir-PS-1** ($TON_{CO_2 \rightarrow CO}$ 6323, $TON_{CO_2 \rightarrow CH_4}$ 1462 and $TON_{CO \rightarrow CH_4}$ (3897). However, **Cu-PS-3** exhibited a gradual decline in photocatalytic activity after 30 hours of continuous irradiation, eventually becoming inactive under prolonged light exposure. This deactivation is attributed to the dissociation of the dimeric species and the concurrent formation of a catalytically inactive Cu(II) state. Overall, this study demonstrates that strategic ligand design and effective metal–ligand cooperativity are key factors in enabling selective and

View Article Online
DOI: 10.1039/D5SC02569B

efficient CH_4 production from CO_2 using earth-abundant metal catalysts. The catalytic systems exhibit consistent performance across a variety of photosensitizers and photochemical conditions, underscoring their potential applicability in solar fuel generation.

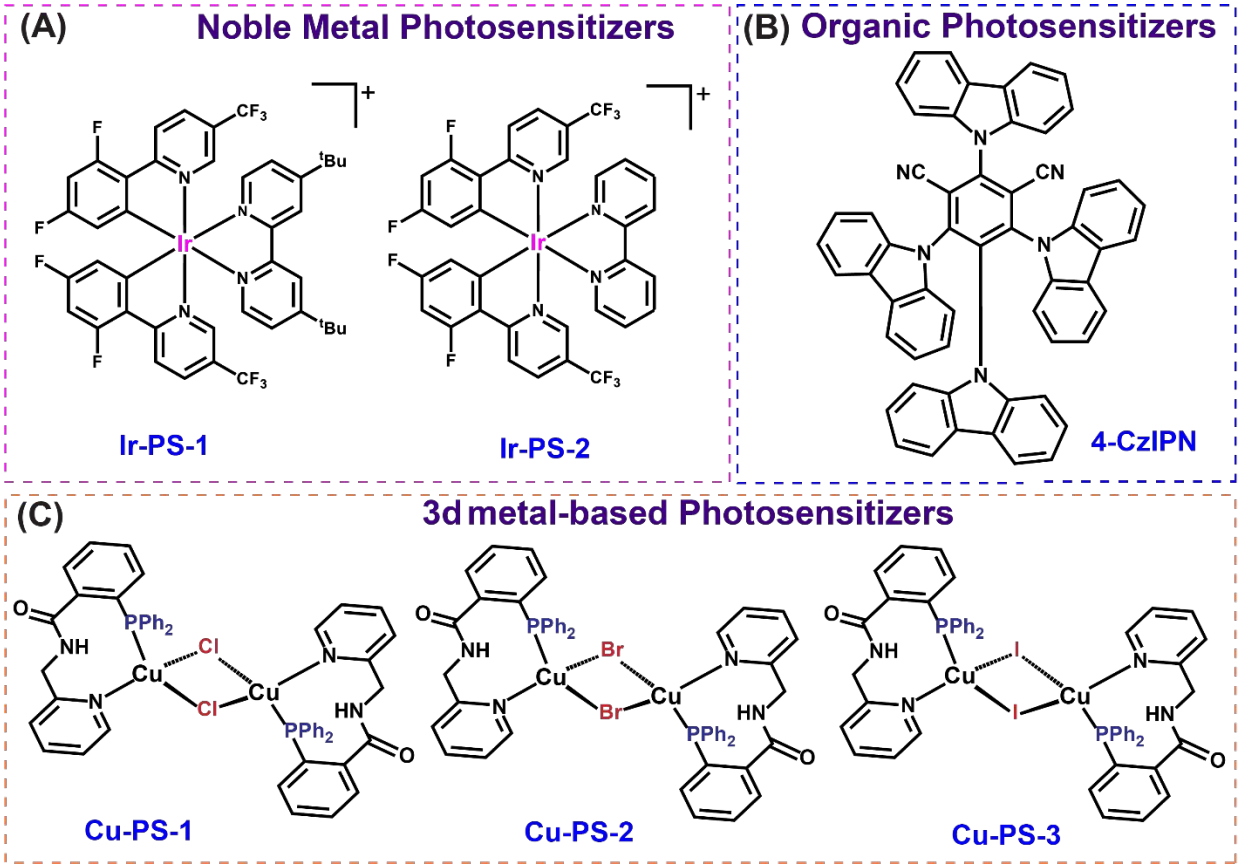

Figure 2. (**A**) Noble-metal Ir-based catalysts: $[Ir\{dF(CF_3)ppy\}_2(bpy)]^+$ and $[Ir\{dF(CF_3)ppy\}_2(dtbbpy)]^+$, (**B**) Organic photosensitizers: 4-CzIPN (1,2,3,5-Tetrakis(carbazol-9-yl)-4,6-dicyanobenzene) (**C**) 3*d* metal-based Cu^I catalysts, $[(CuCl)_2\{PN(H)N\}_2$-κ^2-*P,N*], $[(CuBr)_2\{PN(H)N\}_2$-κ^2-*P,N*] and $[(CuI)_2\{PN(H)N\}_2$-κ^2-*P,N*].

Results and Discussion

To explore the influence of a redox-active ligand in photocatalytic CO_2 to CH_4 conversion, a nickel-based complex (**C1**) was synthesized, incorporating two (6-amino-2(phenylazo)pyridine) [**apap**] as a ligand. The previously reported **apap** ligand was strategically selected due to its electron-rich azo functionality, which promotes efficient intramolecular charge transfer.[43] Additionally, the presence of a free pendant second-sphere amine moiety enables effective proton relay, contributing to enhanced catalytic performance.[43,44] The synthesis of **C1** followed a one-step coordination strategy, where the yellow **apap** ligand was dissolved in dichloromethane (DCM) and treated with 0.5 equivalent $Ni(ClO_4)_2 \cdot 6H_2O$ in a mixture of acetonitrile (ACN) and DCM. To further investigate the role

of the a pendant second-sphere amine group, two additional Ni-based complexes, **C2** and **C3**, were synthesized using [**pap**][43] (2 equivalent) and [**dipap**][45] ligands (1 equivalent), respectively, where the a pendant second-sphere amine functionality is absent in both. The successful formation of all three complexes was initially confirmed by mass spectrometry, with the resulting isotopic patterns aligning well with theoretical predictions (**Figure S1**), and further CNH analysis further confirms the bulk purity of all three complexes (**Figures S2-S4**). Additionally, the complexes exhibited good solubility in polar aprotic solvents, such as dimethyl formamide (DMF), dimethyl sulfoxide (DMSO), and dimethyl acetamide (DMA), facilitating further spectroscopic studies. The preliminary optical study of the complexes was executed in DMA, where three marked absorbance bands were observed between 190 and 1000 nm. To determine the origin of these transitions, optical spectra were acquired for the free [**apap**] ligand. This ligand exhibited a π-π* transition around 300 nm (ε = 5615 $M^{-1}cm^{-1}$) (**Figure S5**). In contrast, the complex **C1** showcased two peaks around 285 nm (ε = 5520 $M^{-1}cm^{-1}$) and 306 nm (ε = 5488 $M^{-1}cm^{-1}$), which appear as a splitting of the ~300 nm peak observed in the ligand, presumably due to the lowering of symmetry (**Figure S5**). Moreover, the free ligand exhibited a peak at ~400 nm for an n-π* transition, while the complex showcased a strong broad band at ~450 nm (ε = 5505 $M^{-1}cm^{-1}$). This band at ~430 nm is assigned to an overlap between ligand-based n-π* and [**apap**] → Ni(II) charge transfer transition (LMCT). The comparative FTIR spectra (**Figure S6A**) of the free **apap** ligand and the **C1** complex displayed a subtle difference in the 3200-3500 cm^{-1} region. Here, the distinct N-H stretching and bending modes of the free ligand disappeared in the **C1** complex, indicating the Ni-N coordination along with the possible hydrogen-bonding interactions.[44] Next, to find out the electronic structure of the distorted tetrahedral Ni(II) complex X-band EPR measurements of the distorted tetrahedral Ni(II) complex were carried out at 77 K, where no signal was observed (**Figure S6B**). This behaviour is typical for high-spin Ni(II) (d^8, S = 1) complexes, particularly those with low-symmetry geometries such as distorted tetrahedral coordination. In such cases, strong zero-field splitting (ZFS) often occurs, which can shift the EPR transitions outside the detectable range or cause significant line broadening, making the signal difficult to observe. Furthermore, fast relaxation processes and low population differences between spin states at 77 K may also suppress the EPR signal. Nevertheless, DFT calculations confirm a high-spin state (S = 1) for the Ni(II) centre, supporting its paramagnetic nature (**Figure S7**). The lack of an experimental EPR signal is therefore attributed to ZFS and relaxation effects rather than the absence of unpaired electrons.[46–52]

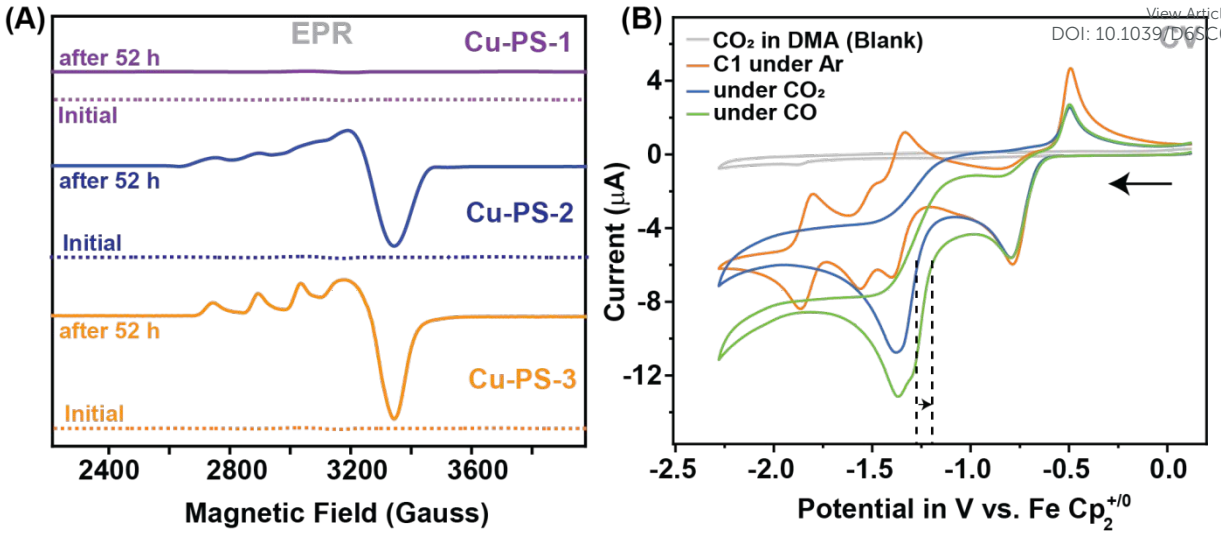

Figure 3. (**A**) The experimental EPR spectrum initial (dotted lines) and after 52 h (solid lines) under irradiation of light spectra of all the Cu^{I}-PS, **Cu^{I}-PS-1** (violet trace), **Cu^{I}-PS-2** (blue trace), **Cu^{I}-PS-3** (orange trace), photosensitizers recorded in DMA at 77 K without irradiation of light. (**B**) Comparative cyclic voltammograms (CVs) of blank DMA (without catalyst) solvent under 1 atmosphere-saturated CO_2 (grey trace), 0.5 mM **C1** under Ar (orange trace), CO_2 (blue trace) atmosphere, and CO (green trace) atmosphere. All the data were recorded in DMA in the presence of 0.1 M $nBu_4N^+BF_4^-$ electrolyte at 0.1 V/s scan rate. The horizontal arrows signify the initial scan direction.

To investigate the role of photosensitizers (PS) in photochemical CO_2 reduction, a series of Ir- and Cu-based PS were synthesized and characterized. The Ir-based photosensitizer **Ir-PS-1** was synthesized following a previously reported procedure.[44] The three Cu(I)-based photosensitizers (**Cu-PS-1, Cu-PS-2,** and **Cu-PS-3**) were synthesized as described in our recent report (**Scheme S1**)[53]. Furthermore, the purity and structural integrity of the synthesized photosensitizers were confirmed by ^{1}H, ^{13}C, and ^{31}P NMR spectroscopy (**Figure S8-S16**).[54] The optical spectra of all the Cu-PS displayed a mixed π–π* and n–π* broad transition at ~320 to ~455 nm in DMA solvent (**Figure S17**). To gain deeper insight into the oxidation state and electronic properties, EPR and cyclic voltammetry (CV) studies were performed. The EPR silence of **Cu-PS-1**, **Cu-PS-2**, and **Cu-PS-3** confirmed that Cu remained in the +1 oxidation state, consistent with its d^{10} electronic configuration represented by a dotted line (**Figure 6A**). Redox behavior was further examined through CV analysis, which revealed distinct Cu(I)/Cu(0) reduction potentials at -1.3 V (**Cu-PS-1**), -1.6 V (**Cu-PS-2**), and -1.7 V (**Cu-PS-3**) vs. $FeCp_2^{+/0}$ (**Figure S18**). The increasing negative shift in redox potential correlated with the halide ligand influence, where Cu-I exhibited the weakest electron affinity, followed by Cu-Br and Cu-Cl, indicating a tunable electronic environment. These findings establish that the Cu-PS complexes are promising alternatives to Ir-based photosensitizers for photochemical CO_2 reduction.

***Electrocatalytic CO_2RR*:** After the preparation of the catalyst **C1**, the redox properties of the catalyst were examined by cyclic voltammetry in DMA media, with all the measured potentials reported against ferrocenium/ferrocene ($FeCp_2^{+/0}$) redox couple. During a cathodic scan ranging from 0.12 V to -2.3 V, **C1** exhibited four electrochemical responses at -0.7 V, -1.35 V, -1.5 V, and -1.8 V under the argon atmosphere (**Figure 3B**, **Figure S19**). Among these signals, the first response at -0.7 V is assigned to the $Ni^{II/I}$ redox process,[21,55,56] while the remaining three signals correspond to ligand-centred redox processes, as confirmed by comparison with a previously reported Zn analogue.[66] To further validate these assignments, in situ spectroelectrochemical optical studies were performed. The emergence of a new peak around 600 nm (under an applied potential of -0.9 V), coupled with the reduction of a peak near 450 nm, confirms the transition from Ni^{II} to Ni^{I} (**Figure S20**).[57] The formation of Ni(I) was further corroborated by EPR spectroscopy, where a rhombic signal was observed with three different g-values ($g_1 = 2.12$, $g_2 = 2.02$, and $g_3 = 1.976$, $g_4 = 1.93$) (**Figure S21A**).[58–60] Additionally, to investigate the ligand-based contribution to the second peak, a similar EPR experiment was conducted at an applied potential of -1.3 V. The resulting spectrum, which shows a g-value of 2.001 along with additional g-values ($g_1 = 2.12$, $g_2 = 2.02$, and $g_4 = 1.93$) (**Figure S21B**), indicates the formation of a radical species along with the Ni(I) state.[58,59,61] Moreover, to corroborate these experimental results, electronic structure calculations were performed. The first one-electron reduction is metal-centred, reducing Ni(II) to Ni(I), as confirmed by molecular orbital (MO) analysis, matching with spin density (S = 1/2) observed in EPR data (<g> = 2.1, Δg = 0.58) (**Figure S21**). The second reduction is ligand-centred, supported by MO/spin density analysis and elongation of the N=N bond to 1.333 Å, indicating the formation of Ni(I)–$L^{\bullet-}$ (**Figure S22**). The resulting doubly reduced intermediate Ni(I)–$L^{\bullet-}$ in **Figure S22** adopts a triplet state (S = 1), which is energetically favoured over the singlet species by 0.6 kcal mol^{-1}. The unpaired electrons are distributed between the metal centre and the ligand. This is corroborated by EPR features (<g> = 2.076, Δg = 0.58; **Figure S21B**), confirming contributions from both centres. Upon introducing CO_2, a sharp increase in reductive current was observed starting at −1.4 V *vs*. $FeCp_2^{+/0,}$ coinciding with the first ligand reduction peak (**Figure 3B**). Upon addition of phenol (PhOH) as an external proton source, the reductive signal increased slightly, consistent with the involvement of proton-coupled electron transfer (PCET) during CO_2 activation (**Figure S19**). Hence, these CV experiments underline the inherent activity of the **C1** complex for electrochemical CO_2 reduction. To assess catalytic activity and product distribution, bulk electrolysis was carried out under CO_2-saturated DMA with phenol

View Article Online
DOI: 10.1039/D6SC02569B

as the proton source at -1.6 V (**Figure S23**). Gas chromatography of the electrochemical cell headspace, following the electrolysis, confirmed the generation of CO and H_2 during electrocatalysis, affording $TON_{CO} \approx 19$ (**Figure S24A**). In contrast, in the absence of a proton source, CO production decreased to $TON_{CO} \approx 12$, underscoring the importance of proton donors in facilitating CO_2 reduction. To further assess the reactivity of **C1** toward CO activation, CV experiments were performed under 1 atm CO in DMA. A distinct reductive wave at −1.25 V was observed, which intensified upon addition of phenol, indicating enhanced CO reduction (**Figure 3B, Figure S19**). Bulk electrolysis of **C1** under CO-saturated DMA with phenol at −1.5 V vs $FeCp_2^{+/0}$ (**Figure S23**) yielded CH_4 and H_2 as gaseous products, with $TON_{CH4} \approx 16$. In the absence of phenol, CH_4 formation was markedly lower ($TON_{CH4} \approx 9$), confirming the critical role of proton transfer in enabling multi-electron CO reduction to CH_4. Electrochemical evaluation of **C2** and **C3** revealed increased current densities under CO_2 compared to Ar, with onset potentials of −1.45 V (**C2**) and −1.48 V (**C3**), suggesting CO2RR activity (**Figures S25–S26**). However, bulk electrolysis produced only modest amounts of CO ($TON_{CO} \approx 6$ for **C2**; ≈ 2 for **C3**), and phenol addition had no measurable effect on product distribution. Together, these results highlight the unique contribution of the pendant amine group in **C1**, which likely engages in proton-coupled electron transfer (PCET) to stabilize reduced Ni intermediates and promote selective CO2RR. The absence of this feature in **C2** and **C3** correlates with diminished activity and efficiency. While **C1** exhibits intrinsic competence for CO_2 and CO reduction, its comparatively modest turnover under electrochemical conditions suggests that the distinct reaction environment under photocatalytic conditions, including the reducing power of the photosensitizer, proton availability, and PCET processes, plays an important role in promoting selective CO and CH_4 production.

***Photocatalytic CO_2RR*:**

Building on the electrochemical CO_2 reduction studies, the photocatalytic performance of **C1** was evaluated under visible-light irradiation in CO_2-saturated, proton-enriched DMA solvent using BIH with 10% v/v TEOA as the sacrificial electron donor (SED). A series of photosensitizers (PS) were systematically screened, including **Ir-PS-1**, **Ir-PS-2**, **CzIPN**, and the Cu(I)-based dimers **Cu-PS-1**, **Cu-PS-2**, and **Cu-PS-3** (**Figure 2**). Prior to photocatalytic testing, cyclic voltammetry and optical spectroscopy were employed to establish the redox potentials and absorption profiles of the PSs (**Figures S27–S29**). Fluorescence quenching experiments were subsequently performed to probe excited-state electron transfer processes.

BIH efficiently quenched the steady-state photoluminescence (PL) of all PSs (**Figures 4, S30–S32**), confirming rapid photoinduced electron transfer from BIH to the excited PS. In contrast, incremental addition of **C1** produced negligible quenching of PL intensity (**Figures 4, S33–S34**). These results rule out direct excited-state energy or electron transfer from the PS to **C1**. Instead, the data support a mechanism in which the reduced PS, generated by reductive quenching with BIH, serves as the effective electron donor to **C1**, thereby initiating the photocatalytic CO_2 reduction cycle.

Optimized Photocatalytic Conditions and Selectivity:

Photochemical CO_2 reduction experiments were performed in a gas-tight quartz vessel under monochromatic 440 nm irradiation and systematically optimized by varying the PS, SED, proton source, and other parameters (**Table S1**). Gaseous products were analyzed by gas chromatography, while the liquid phase was probed using ion chromatography and NMR spectroscopy. The dominant products were CO and CH_4, with only trace H_2 observed; no liquid products were detected. Under optimized conditions with **Ir-PS-1**, **C1** produced CO with a TON of 6323 after 32 h irradiation (**Figures 4A**, **S35**; **Table S1**, entry 8). Intriguingly, prolonged irradiation led to a gradual decline in CO formation accompanied by increased CH_4 production, reaching a TON of 1462 after 68 h with a TOF of 22 h^{-1} (**Figures 4C, S35–S37**). This temporal shift highlights the ability of **C1** to mediate deeper CO_2 reduction, expanding the reduction cycle from CO to CH_4. The addition of an external proton source significantly enhanced activity (**Table S1**, entry 1 vs. entry 8), underscoring the role of the pendant $–NH_2$ group in facilitating proton relay. Systematic variation of phenol concentration revealed that CO production peaked at 0.12 mM (**Figure S38A**). At higher concentrations, CO turnover declined while H_2 generation increased, reflecting competitive proton reduction. CH_4 formation exhibited a stronger dependence on proton concentration relative to CO, consistent with its more demanding $8e^-/8H^+$ pathway versus the $2e^-/2H^+$ requirement for CO formation. Together, these results establish that proton availability critically governs product selectivity, while the $–NH_2$ group within **C1** promotes intramolecular hydrogen bonding and accelerates PCET processes. At excessive proton loadings, this advantage shifts toward parasitic H_2 evolution, revealing a delicate balance between proton concentration and selective CO_2-to-CO/CH_4 conversion.

View Article Online
DOI: 10.1039/D6SC02569B

Comparison with C2 and C3 and the Critical Role of the -NH_2 Group:

To delineate the role of the a pendant second-sphere amine ($-NH_2$) group in secondary coordination sphere interactions, photocatalytic CO_2 reduction was evaluated with **C2** and **C3** under conditions identical to those used for **C1**. In sharp contrast, both **C2** and **C3** selectively generated CO, with TON values of 2758 (**C2**, 68 h) and 2251 (**C3**, 68 h) (**Table S1**, entries 24 and 28; **Figures S39–S40**). Importantly, variation in proton source concentration produced no measurable effect on CO output (**Figures S38** *vs* **S41**), confirming the inability of these catalysts to access deeper reduction pathways beyond CO formation. This divergence highlights the critical function of the pendant $-NH_2$ group in **C1**. Its presence not only enhanced CO_2-to-CO turnover (~5-fold higher TON compared to **C2** and **C3**) but also uniquely enabled CH_4 production, a transformation absent in the control complexes. The ability of **C1** to engage in PCET via intramolecular proton relay appears decisive in lowering barriers for multi-electron reduction beyond the $2e^-/2H^+$ step. These findings firmly establish **C1** as a selective and efficient photocatalyst, with secondary coordination sphere engineering serving as a powerful lever for tuning product distribution. Achieving visible-light-driven CO_2-to-CH_4 conversion, a rare outcome for molecular *3d*-metal catalysts, demonstrates the potential of rational ligand design in orchestrating complex multi-electron photochemical processes. Moreover, the pronounced dependence of product selectivity on proton availability provides guiding principles for the design of next-generation photocatalysts aimed at efficient solar-to-fuel conversion. Building on this foundation, the system was next examined with organic and *3d*-metal-based photosensitizers (PSs) to eliminate reliance on noble-metal PSs. In the presence of **CzIPN**, **C1** exhibited CO production with a TON of 3634 after 32 h (**Table S1**, entry 11; **Figures 4A**, **S42**). As observed with Ir-based systems, CO turnover decreased over time, while CH_4 formation increased, reaching $TON_{CH4} \approx 498$ after 68 h (**Figures 4B**, **S42**). Although organic PSs such as **CzIPN** provide a cost-effective alternative to noble-metal-based PSs, their moderate catalytic activity and limited photostability remain major drawbacks, motivating the exploration of *3d*-metal-based PSs.

Copper Photosensitizers-Performance and Selectivity:

Three dimeric Cu(I) PSs (**Cu-PS-1, Cu-PS-2, Cu-PS-3**) bearing halogen bridges (Cl, Br, I) were evaluated for CO2RR. **Cu-PS-1** showed the highest activity, producing CO with TON ≈ 4789 (**Table S1**, entry 12; **Figures 4A**, **S43**) and CH_4 with TON ≈ 1130 after 68 h (**Figures 4B**, **S43**). **Cu-PS-2** produced CO with TON ≈ 4007 and CH_4 with TON ≈ 642 (**Table S1**, entry

View Article Online
DOI: 10.1039/D5SC02569B

13; **Figures 4A–B**, **S44**), whereas **Cu-PS-3** was significantly less active ($TON_{CO} \approx 257$; $TON_{CH4} \approx 364$) (**Table S1**, entry 16; **Figures 4A–B**, **S45**). Notably, **Cu-PS-2** and **Cu-PS-3** deactivated after 62 h and 42 h, respectively, accompanied by visible solution colour changes, while **Cu-PS-1** retained activity beyond 68 h without degradation.

Mechanistic Insights into Cu(I) PS Deactivation:

In situ EPR, ^{1}H NMR, and $^{31}P\{^{1}H\}$ NMR revealed progressive conversion of Cu^{I}-X-Cu^{I} dimers (X= I, Br) to Cu(II) species during extended irradiation, particularly for **Cu-PS-3**. Broadening and disappearance of NMR signals (**Figures S46–S53**) and the emergence of paramagnetic EPR features ($g \approx 2.1$, hyperfine splitting for I = 3/2; **Figure 3A**) confirmed Cu(I)→Cu(II) oxidation. Fluorescence quenching studies further demonstrated the loss of excited-state activity after 62 h (**Figures S32B**, **S54**). DFT calculations provided a mechanistic basis, showing that weaker orbital overlap and lower-lying antibonding orbitals in **Cu-PS-3** facilitate Cu–I bond cleavage upon photoexcitation, triggering deactivation. Among the three Cu(I)-based dimeric photosensitizers (PS), the Cu-halogen bond strength follows the trend: Cu—Cl—Cu >> Cu—Br—Cu > Cu—I—Cu. This is attributed to the poor orbital overlap between the Cu 3*d* orbital and the larger, more diffuse valence *p* orbital of iodine, as well as the lower-lying lowest unoccupied molecular orbital (LUMO or anti-bonding orbital) of **Cu-PS-3**, as revealed by DFT calculations. Upon photoirradiation, electron excitation into this antibonding orbital leads to cleavage of the Cu-I-Cu bridging bond. Consequently, the Cu(I) centre is oxidized to Cu(II), resulting in the loss of photosensitizer properties and termination of CO_2 reduction activity. This deactivation pathway is supported by EPR spectroscopy (**Figure S55**). It was previously discussed that the lifetime of triplet excited states of Cu(I) systems, having a d^{10} configuration, is much longer than that of Cu(II) systems. Hence, the Cu(I) acts as a photosensitizer. These findings establish **Cu-PS-1** as the most efficient and stable photosensitizer, maintaining long-term catalytic activity without significant structural degradation. In contrast, **Cu-PS-3** deactivates due to Cu(I)→Cu(II) conversion, triggered by weak Cu-I bonds and LUMO-mediated bond cleavage. The combined EPR, NMR, fluorescence, and DFT results highlight fundamental structure-stability relationships and provide design principles for next-generation Cu-based photosensitizers for sustainable CO2RR.

***Photocatalytic CO reduction reaction (CORR)*:**

View Article Online
DOI: 10.1039/D5SC02569B

During extended photochemical CO_2 reduction (>32 h), a striking shift in product selectivity was observed: in situ-generated CO was progressively consumed and converted into CH_4. This observation motivated a direct evaluation of photocatalytic CO reduction (CORR) under otherwise identical conditions, substituting CO for CO_2 as the feedstock. Remarkably, CH_4 formation was significantly enhanced, with TON_{CH4} values substantially exceeding those obtained under CO_2-saturated conditions. After 30 h of irradiation, TON_{CH4} values reached 3897 (**Ir-PS-1**), 3685 (**Ir-PS-2**), 1250 (**CzIPN**), 3102 (**Cu-PS-1**), 1587 (**Cu-PS-2**), and 784 (**Cu-PS-3**) (**Table S1**, entries 18–26; **Figures 4C-D**, **S56**). These results correspond to an approximate twofold increase in CH_4 production relative to CO_2RR, strongly implicating CO as a more reactive intermediate. Because CO requires fewer proton-electron equivalents for full reduction to CH_4, CORR emerges as the more favourable pathway under photochemical conditions. Given the expected involvement of proton-coupled electron transfer (PCET) during CO hydrogenation, the effect of proton source concentration was systematically probed using **Ir-PS-1**. An optimal concentration of phenol (PhOH) increased $TON_{CO\rightarrow CH4}$ by ~30% compared to reactions without added proton donor (**Table S1**, entries 15 vs 16; **Figure S41**). However, excessive protonation promoted parasitic hydrogen evolution (HER), evidenced by a rise in H_2 production (**Figures S40–S41**), underscoring the delicate balance of proton availability required for selective $6H^+/6e^-$ conversion of CO to CH_4. Finally, to confirm that methane originated exclusively from the CO_2 reduction pathway, isotope-labelling experiments were conducted with $^{13}CO_2$. Gas chromatography–mass spectrometry (GC–MS) analysis of the headspace products revealed the characteristic m/z = 17 signal for $^{13}CH_4$, unambiguously verifying that CH_4 formation derived solely from the introduced CO_2 feedstock (**Figures S57–S59**). To further probe the importance of ligand effects in PCET, photochemical CO reduction experiments were conducted with **C2** and **C3**, which lack the secondary -NH_2 functional group present in **C1**. Strikingly, while **C2** facilitated CH_4 formation with a TON_{CH4} of 88 after 32 hours (**Table S1**; Entries 25-30), **C3** exhibited no activity for CO to CH_4 conversion even in the presence of 0.6 mM phenol as a proton sources, confirming that the a pendant second-sphere amine group plays a pivotal role in facilitating proton transfer during CORR. This result aligns with previous CO_2RR findings, further demonstrating that rational ligand design incorporating proton relays is essential for achieving selective multi-electron CO_2 and CO reduction to CH_4.

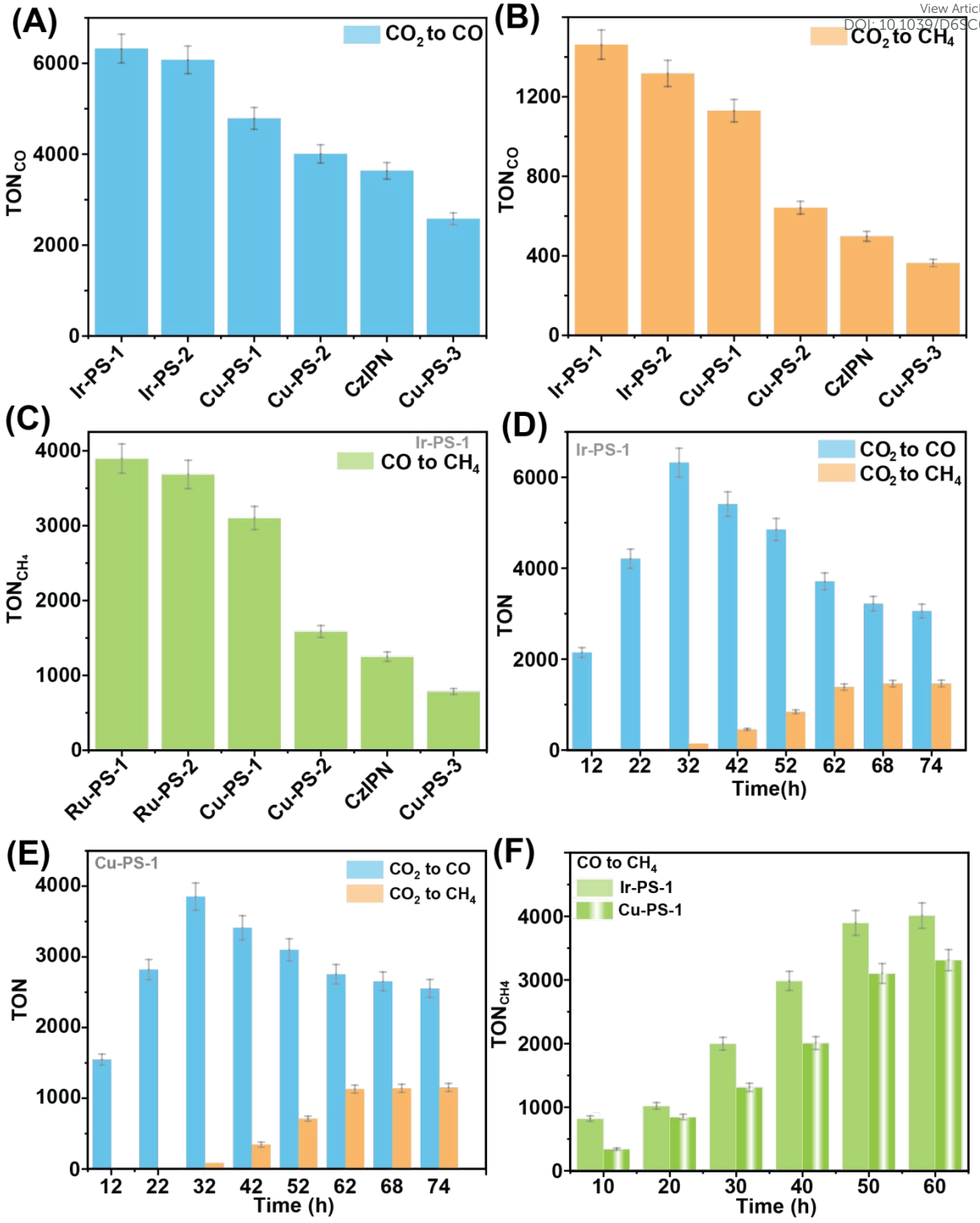

Figure 4. (**A**) Progress of photocatalytic CO_2 to CO conversion and (**B**) CO_2 to CH_4 conversion over time using individual photo-sensitizers **Ir-PS-1**, **Ir-PS-2**, **CzIPN**, **Cu-PS-1**, **Cu-PS-2**, and **Cu-PS-3** along with the catalyst **C1**, phenol as a proton source, and BIH as sacrificial donor in a different photo-setup under irradiation of 440 nm light under CO_2 saturated condition. (**C**) Progress of photocatalytic CO to CH_4 conversion over time using individual photo-sensitizers **Ir-PS-1**, **Ir-PS-2**, **CzIPN**, **Cu-PS-1**, **Cu-PS-2**, and **Cu-PS-3** along with the catalyst **C1**, phenol as a proton source, and as sacrificial donor in a different photo-setup under irradiation of 440 nm light in a CO-saturated condition. (**D** and **E**) The comparative progress of photocatalytic CO_2 to CO and CH_4 in terms of TON in presence of (**D**) **Ir-PS-**

1 and (**E**) 3*d*-metal-based PS, **Cu-PS-1** with the catalyst **C1**, phenol as a proton source, and BIH as sacrificial donor in a different photo-setup under irradiation of 440 nm light under CO_2 saturated condition. (**F**) The comparative progress of photocatalytic CO to CH_4 in terms of TON in presence of **Ir-PS-1** and 3*d*-metal-based PS, **Cu-PS-1** with the catalyst **C1**, phenol as a proton source, and BIH as sacrificial donor in a different photo-setup under irradiation of 440 nm light under CO saturated condition. All the photochemical experiments were carried out under 2 μM catalyst concentration in DMA (2 mL), BIH (0.2 M) as the electron donor, and Photosensitizer (PS) (8 mM), irradiated with a 440 nm LED.

Mechanistic Insight for Electrochemical CO_2/CO to CH_4 via in situ spectroscopic studies:

C1 operates as a dual active catalyst for the transformation of CO_2 and CO to CH_4, functioning under both electrochemical and photocatalytic conditions. Under photochemical conditions, the conversion of the CO_2 to CH_4, whereas in electrochemical conditions, CH_4 formation proceeds through a stepwise pathway involving CO intermediates. In this work, a comprehensive mechanistic framework for the CO_2 to CH_4 conversion is advanced, supported by in situ spectroscopic analyses and corroborated by DFT calculations. A combination of EPR, FTIR, and UV-vis spectroscopy was employed to monitor reaction intermediates under controlled CO_2 and CO atmospheres. Complementary DFT studies elucidated the critical role of the pendant second-sphere amine ($–NH_2$) group, which stabilizes CO_2- and CO-bound intermediates through hydrogen bonding interactions. The catalytic cycle commences with the stepwise two-electron reduction of [NiII$(L)_2$] to the catalytically active [LNi(I)–$L^{\bullet-}$] species **3** (**Figure 6**). The formation of species **3** was established through in situ spectroscopic experiments and supported by DFT analysis (**Figures S21-S22**). Upon exposure to CO_2, nucleophilic attack by **3** on the electrophilic carbon centre of CO_2 yields a CO_2 adduct (species **4**). Protonation of this intermediate generates a Ni–COOH species (**5**), identified by the appearance of a new FTIR band at 1652 cm^{-1}, attributable to the C=O stretch of the Ni-bound COOH moiety (**Figure S60**). Additional vibrational features at 2100 cm^{-1} and 1962 cm^{-1} confirmed the presence of Ni–CO and free CO, respectively (**Figure 5A**).[62] To substantiate these assignments beyond qualitative vibrational analysis, isotopic labelling experiments using $^{13}CO_2$ were performed. Upon replacing $^{12}CO_2$ with $^{13}CO_2$, the CO stretching vibration shifts from 1962 cm^{-1} to 1911 cm^{-1} for the Ni-CO adduct (**Figure S60**), and the COOH-related band shifts from 1652 cm^{-1} for Ni(II)-^{12}COOH to 1598 cm^{-1} the corresponding lower-frequency ^{13}COOH analogue, consistent with the expected isotopic mass effect (**Figure 5C**). These FTIR spectra were recorded under identical conditions at a catalyst concentration of 30 mM, with the $^{12}CO_2$-derived (pink) and $^{13}CO_2$-derived (green) adducts showing clear, systematic isotope-dependent shifts. To further validate formation of the Ni–CO intermediate (**6**), in situ FTIR studies were performed under CO-saturated conditions, revealing a progressive increase in the

View Article Online
DOI: 10.1039/D6SC02569B

1950 cm^{-1} band, consistent with accumulation of Ni–CO species (**Figure 5B**). This conclusion was reinforced by control EPR experiments, wherein exposure of Ni^{I} (**2**) to CO yielded a distinct spectrum diagnostic of Ni–CO formation (species **6**). Once generated, species **6** can either release CO, regenerating the catalyst (CO_2 to CO pathway), or undergo further reduction via a $6H^+/6e^-$ sequential route to CH_4 (CO to CH_4 pathway; **Figure S24B**). The pendant second-sphere amine group plays a pivotal role at this stage, providing a proton relay network that lowers the barrier for CO protonation and facilitates multi-electron reduction. In its absence, as in catalysts **C2** and **C3**, CH_4 formation is markedly suppressed. Stepwise CH_4 evolution proceeds from Ni–CO species **6** through successive two-electron reductions, affording the reduced intermediate **7** (**Figure 6**). Species **7** engages in a proton-coupled electron transfer (PCET) sequence, mediated by $–NH_2$ interactions, to form intermediate **8**. Subsequent PCET steps traverse intermediates **9** and **10**, culminating in the formation of a CH_3-bound Ni^{III} species (**11**), in the catalytic cycle.[58,63] DFT calculations were used to characterize the unstable intermediates **9** and **10**, while EPR spectroscopy provided direct evidence for intermediate **11**. Specifically, EPR spectra recorded under CO-saturated conditions at –1.5 V displayed a distinct signal attributable to $Ni^{III}–CH_3$ (**11**), distinct from previously observed species (**Figure S21E**). Further validation came from chemical oxidation of Ni^{II} to Ni^{III} with ceric ammonium nitrate (CAN), affording an EPR spectrum in excellent agreement with that of species **11** (**Figure S21F**).[58,63] To further validate the formation of the CH_3-bound Ni(III) intermediate under photochemical conditions, a series of key photochemical experiments were conducted in the presence of CO.[64–66] The experiments were performed in a gas-tight quartz vessel under 440 nm visible monochromatic light, employing BIH as an electron donor, **Ir-PS-1** as a photosensitizer, PhOH as a proton source, and 5 equivalents of CH_3I under CO-saturated conditions. The gaseous and liquid products were monitored at different time intervals using gas chromatography (GC) and ion chromatography (IC), respectively. Initially, after 1 hour of irradiation, no detectable gaseous or liquid products were observed. However, after 3 hours, GC analysis revealed the formation of CH_4 and C_2H_6 as the sole gaseous products (**Figure S61**). The production of CH_4 and C_2H_6 continued to increase over time, with a significant rise observed after 6 hours, while no liquid-phase products were detected throughout the experiment. To investigate the mechanistic pathway of C_2H_6 formation, particularly its potential generation via a radical-mediated reaction involving Ni-CH_3 and CH_3I, control experiments were conducted (**Figure S61**). When the reaction was performed in the absence of the catalyst, neither CH_4 nor C_2H_6 was detected. In contrast, when CH_3I was omitted, only CH_4 formation was observed, with no detectable C_2H_6. Collectively, these photochemical and

View Article Online
DOI: 10.1039/D6SC02569B

electrochemical investigations provide compelling evidence that methane formation proceeds through the intermediate species **11** and **12**, supporting the proposed mechanistic framework.

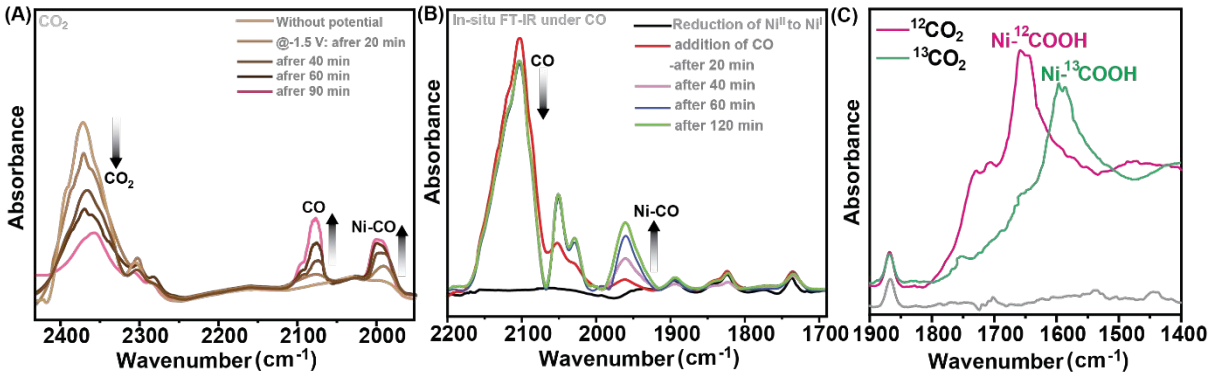

Figure 5. (A) The gradual change in the FTIR spectra of the complex **C1** (30 mM) around 2400-1900 cm^{-1} region during a spectroelectrochemistry experiment in a 100% CO_2 atmosphere executed at -1.6 V *vs.* $FeCp_2^{+/0}$. The vertical arrows highlight the appearance of $\bar{\upsilon}_{CO}$ signal, $\upsilon_{Ni\text{-}CO}$ signals, and simultaneous disappearance of $\bar{\upsilon}_{CO2}$ **(B)** The in-situ generation of the $\upsilon_{Ni\text{-}CO}$ through the purging of CO gas into the DMA solution of one electron reduce species, $[Ni^{I}(pap)_2]$. (**C**) FTIR spectra of Ni(II)-^{12}COOH (1652 cm^{-1}) vs. Ni(II)-^{13}COOH (1598 cm^{-1}) adduct in solvent (catalyst concentration 30 mM). The pink spectra represent the $^{12}CO_2$ adducts of the catalyst C1, and the green ones represent its $^{13}CO_2$ adducts. All data were recorded in DMA media at 298K temperature with a Pt-mesh working electrode, Pt wire counter electrode, and Ag microware pseudo–reference electrode assembled in an OTTLE cell.

As discussed earlier, fluorescence quenching studies were performed to investigate the photocatalytic mechanism involving **C1** using several photosensitizers, including **Ir-based PSs**, **CzIPN**, **Cu-PS-1**, **Cu-PS-2**, and **Cu-PS-3**. The addition of **C1** caused negligible changes in the fluorescence intensity of the photosensitizers, whereas BIH induced significant fluorescence quenching. These results indicate that the photocatalytic reaction proceeds via a reductive quenching pathway, where BIH reductively quenches the excited photosensitizer. To further elucidate the mechanistic details, optical spectroscopic studies were conducted in the presence of the **C1**, **Ir-PS-1**, and BIH under both Ar and CO_2 atmospheres with 440 nm light irradiation. The reaction is initiated by the photoexcitation of $[Ir\text{-}PS\text{-}1]^+$, generating a mixed excited-state involving ^{3}MLCT ($t_{2g}\rightarrow\pi^*_{N=N}$) and ^{3}LC ($\pi_{C=N}\rightarrow\pi^*_{N=N}$) transitions. This excited state undergoes reductive quenching by BIH, resulting in the formation of $[Ir\text{-}PS\text{-}1]^0$ and the oxidized form of BIH ($BIH^{\bullet+}$), which rapidly deprotonates to form $BI^{\bullet}$. The radical species $BI^{\bullet}$ is a highly reducing intermediate (E_0 ($BI^{\bullet}/BI^+$) = −2.06 V *vs.* $FeCp_2^{+/0}$) and can subsequently reduce another molecule of $[Ir\text{-}PS\text{-}1]^+$, yielding two equivalents of $[Ir\text{-}PS\text{-}1]^0$ in the overall photoinduced process.[29,30,67,68] The reduced $[Ir\text{-}PS\text{-}1]^0$ species serves as an electron donor to facilitate the stepwise reduction of **C1** and generate $[Ni^{I}(APAP^{\bullet-})]$. The appearance of a new absorption peak around 600 nm in the optical spectra recorded under an Ar atmosphere after 3 hours of light irradiation indicates the reduction of Ni(II) to Ni(I). This reduction was further

corroborated by spectroelectrochemical studies, where a similar absorption feature emerged upon applying a potential of -0.95 V vs. $FeCp_2^{+/0}$. The consistency of this spectral signature under both photochemical (**Figure S62A**) and electrochemical (**Figure S62B**) conditions provides strong evidence that Ni(II) reduction to Ni(I) occurs via the reductive quenching of **Ir-PS-1**. Interestingly, under identical photocatalytic conditions in the presence of CO_2, the diminishing peak intensity around 600 nm, accompanied by the simultaneous emergence of a new peak in the 500–550 nm region, confirms the formation of a CO_2 adduct species. However, the CV studies under Ar vs. CO_2 and our previously reported Cu-based analogoes depict the CO_2RR going through a ligand-induced, metal-based pathway.[43] Upon light irradiation, similar to **Ir-PS-1**, **Cu-PS-1** undergoes photoexcitation to its triplet excited state, $^3[Cu^I\text{-PS}]^*$, which is subsequently quenched by BIH, forming an unstable reduced species. This reduced species then undergoes sequential electron transfer steps and forms $[Ni(II)(L)_2]$ to $[LNi(I)–L^{\bullet-}]$. Thus, the catalytic cycle begins with the successive two-electron reduction of the Ni(II) centre and the ligand moiety, generating the intermediate species **3** through the reductive quenching of the photosensitizer (PS). Next, in the presence of CO_2, the reduced species **C** reacts with CO_2 to form a CO_2 adduct species **4**, as confirmed by in situ optical spectroscopic studies under identical photochemical conditions. Species **4** then undergoes a proton-coupled electron transfer (PCET) pathway, leading to the formation of a CO-bound Ni species **6** followed by intermediate species **5**, accompanied by the elimination of H_2O. The resulting Ni^{II}-CO intermediate can either release CO, regenerate the Ni(II) catalyst, or proceed through a $6e^-/6H^+$ reduction pathway, ultimately forming CH_4 as the final product.

Moreover, to further investigate whether the observed photocatalytic activity originates from molecular Ni species or from any in situ generated metallic Ni nanoparticles, mercury (Hg) poisoning experiments were performed during photocatalysis. Mercury is known to selectively amalgamate with metallic nanoparticles, thereby suppressing heterogeneous metal-mediated catalytic pathways. Under Hg-treated conditions, the TON values for both CO and CH_4 formation exhibited only a marginal decrease (<5%) compared to the standard reaction conditions (**Figure S63**). This minimal change indicates that heterogeneous Ni-based species, if formed at all, contribute negligibly to the overall catalytic performance. To further verify the absence of nanoparticle formation, dynamic light scattering (DLS) analyses were conducted during the photocatalytic reaction to monitor the possible generation of colloidal or particulate species. Importantly, no detectable nanoparticles or aggregates were observed throughout the course of catalysis (**Figure S64**). Collectively, the Hg poisoning experiments together with the

View Article Online
DOI: 10.1039/D5SC02569B

DLS analyses strongly support that the photocatalytic CO_2 reduction in this system proceeds predominantly through a homogeneous molecular Ni catalytic pathway, with no evidence for the formation of catalytically active Ni nanoparticles under the applied experimental conditions.

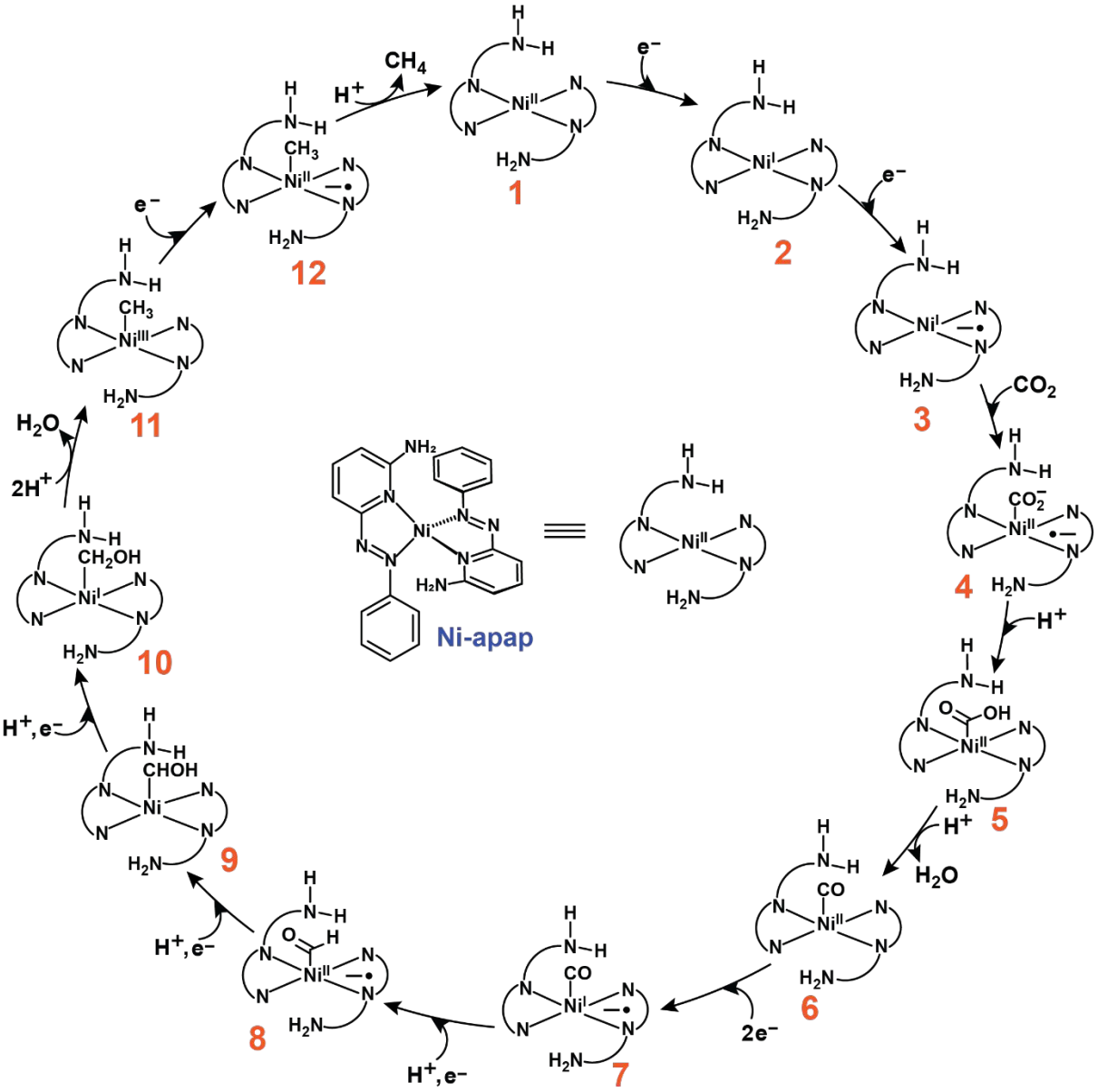

Figure 6. A probable mechanistic pathway for CO_2 to CH_4.

Mechanistic Insight for Electrochemical CO_2/CO to CH_4 in the light of DFT Calculation:

The first electron reduction is metal-centred, converting Ni^{II} to Ni^{I}. DFT analysis of molecular orbitals and spin density distributions (**Figure S22**) indicates spin localization at the Ni centre, consistent with an S = 1/2 state. This assignment is corroborated by the EPR spectrum of the reduced complex, which exhibits a rhombic signal (g = 2.1, Δg = 0.58; **Figure S21**). The second

View Article Online
DOI: 10.1039/D6SC02569B

reduction is ligand-centred, generating the NiI–$L^{\bullet-}$ species. MO and spin density analyses, together with elongation of the N=N bond from 1.269 to 1.333 Å, support occupation of the azo π^* orbital. The doubly reduced species (**3**) adopts a triplet ground state (S = 1), which is favoured by 0.6 kcal mol^{-1} over the singlet counterpart. This configuration corresponds to independent spin localization on the Ni^{I} centre and the azo-functionalized ligand. The electronic arrangement is further supported by EPR spectroscopy, which shows a signal at g = 2.076 with Δg = 0.58 (**Figure S21**). CO_2 activation proceeds via electron transfer from Ni^{I} to the substrate, affording a Ni^{II}–$CO_2^{\bullet-}$ adduct (**4**). Protonation at the pendant –NH_2 group produces a hydrogen-bonded [4+H^+] species, where the CO_2 radical anion is stabilized by an O···H–N interaction of 1.636 Å. This interaction promotes formation of the Ni–COOH intermediate (5) through **TS1** with a computed barrier of 1.83 kcal mol^{-1} (**Figure 7**). Intermediate **5** is further stabilized by intramolecular hydrogen bonding between the carboxyl oxygen and the ligand –NH group (1.756 Å), underscoring the critical role of the pendant amine in consolidating reactive intermediates. The Ni–COOH species undergoes protonation and water elimination to generate the Ni–CO adduct (**6**), completing the two-electron reduction of CO_2 to CO. The catalytic cycle then extends beyond CO formation. A second two-electron reduction ($Ni^{II} \rightarrow Ni^{I}$ and $L \rightarrow L^{\bullet-}$) affords intermediate **7** in a triplet spin state (S = 1), favoured by 12 kcal mol^{-1} relative to the singlet state. Intermediate **7** engages in PCET via **TS2** to form **8**, corresponding to the formal reduction of –CO to –CHO, as supported by elongation of the C–O bond (**Figure 7**). A subsequent PCET step converts **8** to **9** via **TS3**, which then undergoes further reduction and protonation to afford **10** (**Figure 7**). Protonation of **10**, accompanied by water elimination, generates the Ni^{III}–CH_3 intermediate (**11**). DFT calculations assign a quartet spin state (S = 3/2), more stable than the corresponding doublet by 26.8 kcal mol^{-1} (**Figure S65**). The Ni oxidation state in **11** is assigned as Ni^{III}, supported by in situ EPR spectroscopy, which displays diagnostic features distinct from other Ni species (**Figure S21E–F**). A final one-electron reduction of **11** yields intermediate **12**, which upon protonation, releases CH_4 as the terminal product and regenerates the catalytically active species **1**. Notably, photochemical studies reveal that the same intermediates are accessed under light-driven conditions. Under CO-saturated irradiation at 440 nm in the presence of CH_3I, BIH, **Ir-PS-1**, and PhOH; CH_4 and C_2H_6 were the only gaseous products observed (**Figure S61**). Control experiments established that C_2H_6 arises from radical coupling between Ni–CH_3 and CH_3I, whereas omission of CH_3I yielded only CH_4. These observations provide direct experimental support for Ni^{III}–CH_3 (**11**) as a key intermediate under both electrochemical and photochemical regimes. Taken together, the combined DFT and spectroscopic data converge on a unified mechanistic framework for

View Article Online
DOI: 10.1039/D5SC02569B

CO_2-to-CH_4 conversion. In this pathway, the pendant $–NH_2$ group serves as a proton relay, stabilizing reactive intermediates and lowering barriers for PCET events, while cooperative metal–ligand redox activity orchestrates the multielectron sequence. Importantly, the same mechanistic principles apply under electrochemical and photochemical conditions, underscoring the generality of **C1** as a dual-active catalyst for selective CH_4 evolution.

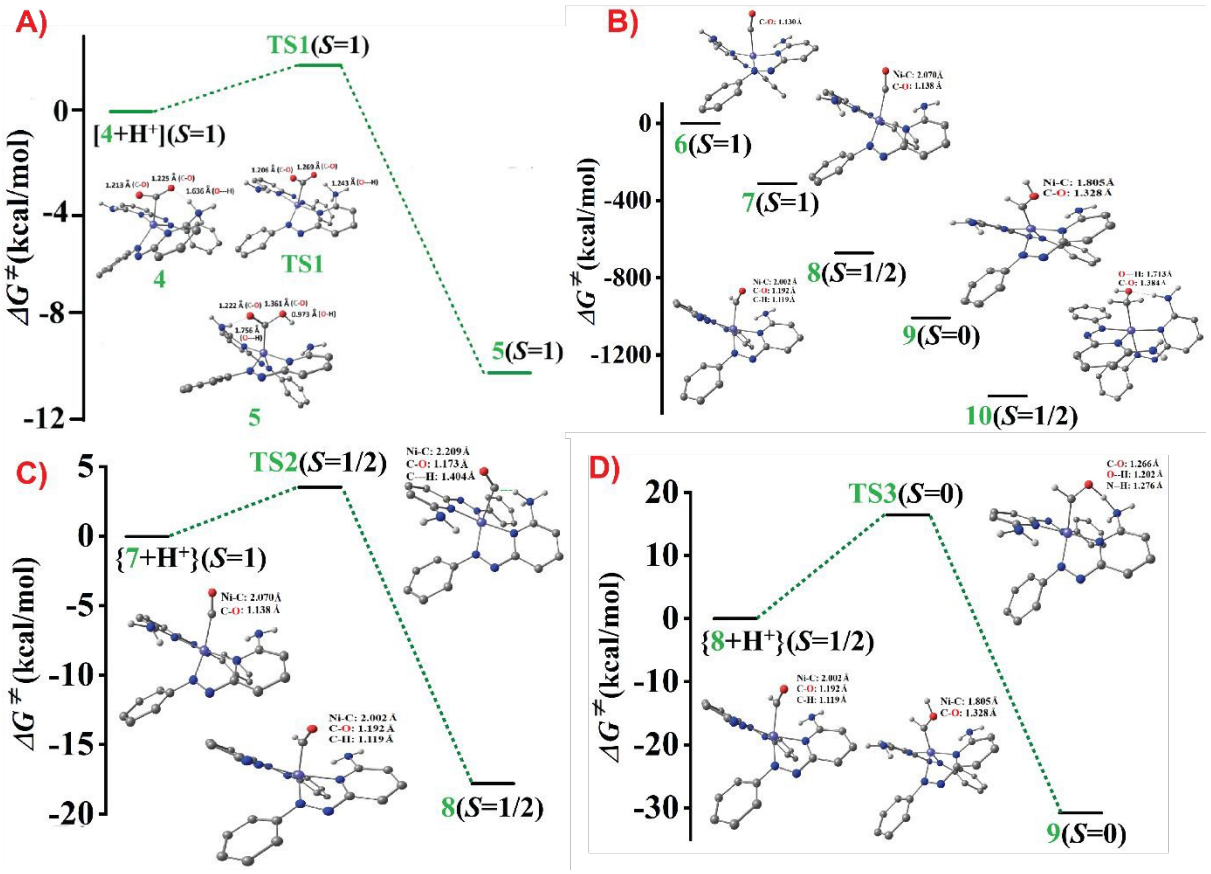

Figure 7. (**A**, **C**, and **D**) The optimized geometry of transition state **TS2** highlights a significant secondary coordination sphere coordination sphere effect, characterized by a secondary hydrogen-bonding interaction between the free $–NH_2$ group and the Ni-coordinated CO_2 molecule. Relative energies of the various spin states are reported in kcal/mol. All bond distances are given in Å. For clarity, hydrogen atoms are omitted from the structures except for those bonded to the free $–NH_2$ group. (**B**) Gibbs free energy diagram (kcal/mol) for DFT-optimized structures of six coordinated CO adducts with the NiL2 complex (**6**) Ni(II)–CO, (**7**) Ni(I)–CO, (**8**) Ni(II)–CHO, (**9**) Ni(II)–CHOH, and (**10**) Ni(I)–CH_2OH. Color codes: carbon → gray, hydrogen→ white, nitrogen → blue, oxygen → red, and nickel → bluish gray.

Conclusion

This work establishes a redox-active (6-amino-2-(phenylazo)pyridine)-nickel complex (**C1**) as an efficient and sustainable molecular platform for the selective reduction of CO_2 to CH_4 under both electrochemical and photochemical conditions. Although electrolysis afforded only

modest activity, coupling **C1** with visible-light photosensitizers and optimized proton/electron sources resulted in dramatic improvements in efficiency and product selectivity. Notably, Cu(I)-based photosensitizers with tuneable halide bridges were identified as effective, earth-abundant alternatives to Ir-systems, with **Cu-PS-1** delivering turnover numbers (TONs) for CO_2-to-CO (4789), CO_2-to-CH_4 (1130), and CO-to-CH_4 (3102) that rival state-of-the-art noble-metal photosensitizers. Comprehensive mechanistic probing, combining DFT with in situ EPR, FT-IR, UV-vis, and electrochemical analyses, revealed that catalysis proceeds through a cooperative metal-ligand redox pathway. The Ni centre and azo-functionalized ligand undergo sequential reductions to generate a Ni–CO_2 adduct, followed by proton-coupled electron transfer steps leading to CH_4. Crucially, the pendant –NH_2 functionality facilitates hydrogen bonding to stabilize key COOH and CH_x intermediates and lowers kinetic barriers along the multielectron pathway. Direct detection of a Ni^{III}–CH_3 species provides experimental support for C–H bond formation as the final step in methane evolution, with identical intermediates observed under both electrochemical and photochemical regimes. Together, these findings define a unified mechanistic framework for **C1**-mediated CO_2 reduction and underscore the broader potential of redox-active ligand scaffolds in molecular catalyst design. By demonstrating that earth-abundant transition metals, when paired with properly engineered ligands and photosensitizers, can mediate the full eight-electron conversion of CO_2 to CH_4, this study establishes design principles for next-generation systems in artificial photosynthesis and carbon valorization. More broadly, this work highlights the promise of integrating low-cost, tuneable molecular architectures with solar energy input to advance sustainable fuel production and scalable carbon recycling technologies.

Acknowledgements

The authors would like to acknowledge the central instrumental facility and financial support from the Indian Institute of Technology Bombay (IITB). A.D. acknowledges the funding support from DST, India-supported National Centre of Excellence for Carbon Capture, Utilization, and Storage (DST/TMD/CCUS/CoE/202/IITB) and the Ministry of Steel, Government of India (S-20021/19/2024-TECH/19973).

Abbreviations

CO2RR: Carbon-di-oxide reduction reaction

FTIR: Fourier transform infrared spectroscopy

View Article Online
DOI: 10.1039/D6SC02569B

EPR: Electron paramagnetic resonance

TEOA: Triethanolamine

TBABF: Tetrabutylammonium tetrafluoroborate

CCUS: Carbon capture, utilization, and storage

CzIPN: 2,4,5,6-Tetra(9H-carbazol-9-yl)isophthalonitrile

LED: Light-Emitting Diode

PS: Photosensitizer

SED: Sacrificial electron donor

BIH: 3-dimethyl-2-phenyl-2,3-dihydro-1H-benzo[d]imidazole

TON: Turn Over Number

PCET: Proton-coupled electron transfer

DMA: Dimethylacetamide

DFT: Density functional theory

Conflict of Interest

C.D. and A.D. have applied for a provisional Indian Patent (Application Number 2024034835) along with IIT Bombay, with a part of the work reported here.

References:

1 D. Kim, K. K. Sakimoto, D. Hong and P. Yang, *Angewandte Chemie International Edition*, 2015, **54**, 3259–3266.
2 H. B. Gray, *Nature Chem*, 2009, **1**, 7–7.
3 N. S. Lewis and D. G. Nocera, *Proceedings of the National Academy of Sciences*, 2006, **103**, 15729–15735.
4 S. Nitopi, E. Bertheussen, S. B. Scott, X. Liu, A. K. Engstfeld, S. Horch, B. Seger, I. E. L. Stephens, K. Chan, C. Hahn, J. K. Nørskov, T. F. Jaramillo and I. Chorkendorff, *Chem. Rev.*, 2019, **119**, 7610–7672.
5 P. Majumder and A. Dutta, *iScience*, DOI:10.1016/j.isci.2025.113509.
6 P. Kurz, B. Probst, B. Spingler and R. Alberto, *European Journal of Inorganic Chemistry*, 2006, **2006**, 2966–2974.
7 D. Ghosh, T. Kajiwara, S. Kitagawa and K. Tanaka, *European Journal of Inorganic Chemistry*, 2020, **2020**, 1814–1818.
8 H. Shirley, T. M. Sexton, N. P. Liyanage, C. Z. Palmer, L. E. McNamara, N. I. Hammer, G. S. Tschumper and J. H. Delcamp, *European Journal of Inorganic Chemistry*, 2020, **2020**, 1844–1851.

9 B. M. Rosen, K. W. Quasdorf, D. A. Wilson, N. Zhang, A.-M. Resmerita, N. K. Garg and V. Percec, *Chem. Rev.*, 2011, **111**, 1346–1416.
10 W. Keim, *Angewandte Chemie International Edition in English*, 1990, **29**, 235–244.
11 J.-H. Jeoung and H. Dobbek, *Science*, 2007, **318**, 1461–1464.
12 J. Fesseler, J.-H. Jeoung and H. Dobbek, *Angewandte Chemie International Edition*, 2015, **54**, 8560–8564.
13 D. Hong, T. Kawanishi, Y. Tsukakoshi, H. Kotani, T. Ishizuka and T. Kojima, *J. Am. Chem. Soc.*, 2019, **141**, 20309–20317.
14 D. Hong, Y. Tsukakoshi, H. Kotani, T. Ishizuka and T. Kojima, *J. Am. Chem. Soc.*, 2017, **139**, 6538–6541.
15 V. S. Thoi, N. Kornienko, C. G. Margarit, P. Yang and C. J. Chang, *J. Am. Chem. Soc.*, 2013, **135**, 14413–14424.
16 H. Shirley, X. Su, H. Sanjanwala, K. Talukdar, J. W. Jurss and J. H. Delcamp, *J. Am. Chem. Soc.*, 2019, **141**, 6617–6622.
17 E. Kimura, X. Bu, M. Shionoya, S. Wada and S. Maruyama, *Inorg. Chem.*, 1992, **31**, 4542–4546.
18 C. A. Craig, L. O. Spreer, J. W. Otvos and Melvin. Calvin, *J. Phys. Chem.*, 1990, **94**, 7957–7960.
19 J. Schneider, H. Jia, K. Kobiro, D. E. Cabelli, J. T. Muckerman and E. Fujita, *Energy & Environmental Science*, 2012, **5**, 9502–9510.
20 B. J. Fisher and R. Eisenberg, *J. Am. Chem. Soc.*, 1980, **102**, 7361–7363.
21 X. Su, K. M. McCardle, J. A. Panetier and J. W. Jurss, *Chem. Commun.*, 2018, **54**, 3351–3354.
22 M. F. Kuehnel, K. L. Orchard, K. E. Dalle and E. Reisner, *J. Am. Chem. Soc.*, 2017, **139**, 7217–7223.
23 J. Lin, B. Qin and Z. Fang, *Catal Lett*, 2019, **149**, 25–33.
24 H.-H. Huang, J.-H. Zhang, M. Dai, L. Liu, Z. Ye, J. Liu, D.-C. Zhong, J.-W. Wang, C. Zhao and Z. Ke, *Proceedings of the National Academy of Sciences*, 2022, **119**, e2119267119.
25 N.-X. Li, Y.-M. Chen, Q.-Q. Xu and W.-H. Mu, *Journal of CO2 Utilization*, 2023, **68**, 102385.
26 J. Zhang, P. She, Q. Xu, F. Tian, H. Rao, J.-S. Qin, J. Bonin and M. Robert, *ChemSusChem*, 2024, **17**, e202301892.
27 H. Rao, L. C. Schmidt, J. Bonin and M. Robert, *Nature*, 2017, **548**, 74–77.
28 H. Rao, C.-H. Lim, J. Bonin, G. M. Miyake and M. Robert, *J. Am. Chem. Soc.*, 2018, **140**, 17830–17834.
29 A. Rosas-Hernández, P. G. Alsabeh, E. Barsch, H. Junge, R. Ludwig and M. Beller, *Chem. Commun.*, 2016, **52**, 8393–8396.
30 M. S. Lowry, J. I. Goldsmith, J. D. Slinker, R. Rohl, R. A. Pascal, G. G. Malliaras and S. Bernhard, *Chem. Mater.*, 2005, **17**, 5712–5719.
31 T. Bortolato, S. Cuadros, G. Simionato and L. Dell'Amico, *Chemical Communications*, 2022, **58**, 1263–1283.
32 H. Yuan, Y. Yu, S. Yang, Q. Lei, Z. Yang, B. Lan and Z. Han, *Chemical Communications*, 2024, **60**, 6292–6295.
33 Y. Wang, L. Chen, T. Liu and D. Chao, *Dalton Transactions*, 2021, **50**, 6273–6280.
34 J. Bonin, M. Robert and M. Routier, *J. Am. Chem. Soc.*, 2014, **136**, 16768–16771.
35 J.-W. Wang, F. Ma, T. Jin, P. He, Z.-M. Luo, S. Kupfer, M. Karnahl, F. Zhao, Z. Xu, T. Jin, T. Lian, Y.-L. Huang, L. Jiang, L.-Z. Fu, G. Ouyang and X.-Y. Yi, *J. Am. Chem. Soc.*, 2023, **145**, 676–688.
36 W. Helweh, P. Kim, Z. J. Mast, B. T. Phelan, N. P. Weingartz, R. Zong, S. Chaudhuri, R. P. Thummel, G. C. Schatz and L. X. Chen, *Inorg. Chem.*, DOI:10.1021/acs.inorgchem.4c01251.
37 M. M. Alowakennu, A. Ghosh and J. K. McCusker, *J. Am. Chem. Soc.*, 2023, **145**, 20786–20791.
38 K. Kiyosawa, N. Shiraishi, T. Shimada, D. Masui, H. Tachibana, S. Takagi, O. Ishitani, D. A. Tryk and H. Inoue, *J. Phys. Chem. C*, 2009, **113**, 11667–11673.
39 N. Nagata, Y. Kuramochi and Y. Kobuke, *J. Am. Chem. Soc.*, 2009, **131**, 10–11.
40 M. C. Rosko, K. A. Wells, C. E. Hauke and F. N. Castellano, *Inorg. Chem.*, 2021, **60**, 8394–8403.
41 H. Takeda, K. Ohashi, A. Sekine and O. Ishitani, *J. Am. Chem. Soc.*, 2016, **138**, 4354–4357.
42 S. Patra, S. Bhunia, S. Ghosh and A. Dey, *ACS Catal.*, 2024, **14**, 7299–7307.

43 S. Guria, D. Dolui, C. Das, S. Ghorai, V. Vishal, D. Maiti, G. K. Lahiri and A. Dutta, *Nat Commun*, 2023, **14**, 6859.
44 C. Das, S. Ghosh, A. Guha, P. Majumder, G. K. Lahiri and A. Dutta, *Crystal Growth & Design*, DOI:10.1021/acs.cgd.4c00756.
45 C. Das, S. Ghosh, R. Biswas, G. K. Lahiri and A. Dutta, *Chemical Communications*, 2024, **60**, 10492–10495.
46 G. Musie, P. J. Farmer, T. Tuntulani, J. H. Reibenspies and M. Y. Darensbourg, *Inorg. Chem.*, 1996, **35**, 2176–2183.
47 P. Prabukanthan, M. Sreedhar, S. Thamaraiselvi, G. Harichandran, P. Seenuvasakumaran, M. M. Hanafiah and C. Fernandez, *J Mater Sci: Mater Electron*, 2021, **32**, 6331–6343.
48 L. Gomes, E. Pereira and B. de Castro, *Journal of the Chemical Society, Dalton Transactions*, 2000, **0**, 1373–1379.
49 A. Müller, I. Tscherny, R. Kappl, C. E. Hatchikian, J. Hüttermann and R. Cammack, *J Biol Inorg Chem*, 2002, **7**, 177–194.
50 A. K and V. Kathirvelu, *Journal of Physics and Chemistry of Solids*, 2021, **157**, 110224.
51 N. Sarı, S. Ç. Şahin, H. Öğütcü, Y. Dede, S. Yalcin, A. Altundaş and K. Doğanay, *Spectrochimica Acta Part A: Molecular and Biomolecular Spectroscopy*, 2013, **106**, 60–67.
52 K. Thangavel, P. C. Bruzzese, M. Mendt, A. Folli, K. Knippen, D. Volkmer, D. M. Murphy and A. Pöppl, *Phys. Chem. Chem. Phys.*, 2023, **25**, 15702–15714.
53 G. Sabharwal, K. C. Dwivedi and M. S. Balakrishna, *Applied Organometallic Chemistry*, 2025, **39**, e70322.
54 G. Sabharwal, K. C. Dwivedi, C. Das, T. R. K. Rana, A. Dutta, G. Rajaraman and M. S. Balakrishna, *Journal of Catalysis*, 2024, **440**, 115825.
55 J. D. Froehlich and C. P. Kubiak, *J. Am. Chem. Soc.*, 2015, **137**, 3565–3573.
56 T. Fogeron, T. K. Todorova, J.-P. Porcher, M. Gomez-Mingot, L.-M. Chamoreau, C. Mellot-Draznieks, Y. Li and M. Fontecave, *ACS Catal.*, 2018, **8**, 2030–2038.
57 M. Claros, F. Ungeheuer, F. Franco, V. Martin-Diaconescu, A. Casitas and J. Lloret-Fillol, *Angewandte Chemie International Edition*, 2019, **58**, 4869–4874.
58 H. Na and L. M. Mirica, *Nat Commun*, 2022, **13**, 1313.
59 I. E. Soshnikov, N. V. Semikolenova, K. P. Bryliakov, A. A. Antonov, W.-H. Sun and E. P. Talsi, *Journal of Organometallic Chemistry*, 2019, **880**, 267–271.
60 M. Valente, C. Freire and B. de Castro, *J. Chem. Soc., Dalton Trans.*, 1998, 1557–1562.
61 A. Awasthi, I. F. Leach, S. Engbers, R. Kumar, R. Eerlapally, S. Gupta, J. E. M. N. Klein and A. Draksharapu, *Angew Chem Int Ed*, 2022, **61**, e202211345.
62 G. Bender, T. A. Stich, L. Yan, R. D. Britt, S. P. Cramer and S. W. Ragsdale, *Biochemistry*, 2010, **49**, 7516–7523.
63 L. Griego, J. B. Chae and L. Mirica, 2023, preprint, DOI: 10.26434/chemrxiv-2023-fpf1n.
64 G. K. Lahiri, L. J. Schussel and A. M. Stolzenberg, *Inorg. Chem.*, 1992, **31**, 4991–5000.
65 I. Bach, R. Goddard, C. Kopiske, K. Seevogel and K.-R. Pörschke, *Organometallics*, 1999, **18**, 10–20.
66 D. Lexa, J. M. Saveant and D. L. Wang, *Organometallics*, 1986, **5**, 1428–1434.
67 A. P. Wilde, K. A. King and R. J. Watts, *J. Phys. Chem.*, 1991, **95**, 629–634.
68 M. G. Colombo, A. Hauser and H. U. Guedel, *Inorg. Chem.*, 1993, **32**, 3088–3092.

Data Availability Statement

View Article Online
DOI: 10.1039/D6SC02569B

The data supporting this article have been included as part of the Supplementary Information.